ADVANCING EARTH AND SPACE SCIENCES

Geophysical Research Letters

RESEARCH LETTER
10.1029/2024GL109517

Quantifying Earth's Topography: Steeper and Larger Than Projected in Digital Terrain Models

Anne Voigtländer[1,2], Aljoscha Rheinwalt[3], and Stefanie Tofelde[4]

[1]Geomorphology, Helmholtz Centre Potsdam - GFZ German Research Centre for Geosciences, Potsdam, Germany, [2]Lawrence Berkeley National Laboratory, Energy Geosciences Division, Berkeley, CA, USA, [3]University of Potsdam, Institute of Geosciences, Geological Remote Sensing, Potsdam, Germany, [4]Freie Universität, Institute of Geological Sciences, Tectonics and Sedimentary Systems, Berlin, Germany

Anne Voigtländer, Aljoscha Rheinwalt, and Stefanie Tofelde contributed equally to this work.

Key Points:

- The projection error in gridded models biases our view of surface topography at all scales
- Correcting for the projection error allows exploring physics-based erosion and transport laws
- The correction enables better sourcing of the topographic data we have access to

Supporting Information:

Supporting Information may be found in the online version of this article.

Correspondence to:

A. Voigtländer,
anne.voigtlaender@gfz-potsdam.de

Citation:

Voigtländer, A., Rheinwalt, A., & Tofelde, S. (2024). Quantifying Earth's topography: Steeper and larger than projected in digital terrain models. *Geophysical Research Letters*, *51*, e2024GL109517. https://doi.org/10.1029/2024GL109517

Received 29 MAR 2024
Accepted 26 JUN 2024

Author Contributions:

Conceptualization: Anne Voigtländer, Stefanie Tofelde
Data curation: Aljoscha Rheinwalt, Stefanie Tofelde
Formal analysis: Anne Voigtländer, Aljoscha Rheinwalt
Investigation: Anne Voigtländer, Stefanie Tofelde
Methodology: Anne Voigtländer, Aljoscha Rheinwalt, Stefanie Tofelde
Resources: Anne Voigtländer, Stefanie Tofelde
Software: Aljoscha Rheinwalt
Supervision: Anne Voigtländer
Validation: Anne Voigtländer
Visualization: Anne Voigtländer, Aljoscha Rheinwalt, Stefanie Tofelde

Abstract Grid- or pixel-based models, used across various scientific disciplines from microscopic to planetary scales, contain an unquantified error that bias our interpretation of the data. The error is produced by projecting 3D data onto a 2D grid. For Digital Terrain Models (DTMs) the projection error affects all slope-dependent topographic metrics, like surface area or slope angle. Due to the proportionality of the error to the cosine of the slope, we can correct for it. We quantify the error and test the correction using synthetic landscapes for which we have analytical solutions of their metrics. Application to real-world landscapes in California, reveal the systematic underestimation of surface area by up to a third, and mean slope angles by up to 10° in steep topography in current DTMs. Correcting projection errors allow for true estimates of surface areas and slope distributions enabling physics-based models of surface processes at any spatial scale.

Plain Language Summary Hiking up a steep mountain slope feels longer than the horizontal distance measured on a map. The slope angle is calculated by taking the height over the horizontal distance. The length of a (mountain) slope is always greater than the horizontal plane. This mistake is also very common in Digital Terrain Models (DTMs). Here landscapes images captured in a bird's eye view are projected onto horizontal gridded surfaces. In the model, each grid cell has the same length and contains the height of the landscape. Due to the view, the slopes are only represented by the horizontal distance, which is shorter. We call this the projection error. Because the error depends on the slope, we use it to fix it. We test the correction on different landscapes with steep and gentle topography. We find that uncorrected models underestimate surface area and length by up to a third. Fixing the projection error shows that mountain slopes are much steeper and longer than usually reported. Knowing the true length of a mountain slope, we can use the topographic data to better understand and maybe predict processes and volumes, like landslides or fluid transport.

1. Introduction

Advancements in remote sensing techniques and computing provide accessibility and scalability to probe surface topographies from nano- to planetary-scale across all Sciences (Brodsky et al., 2016; Burbank et al., 1996; Church, 2010; DiBiase et al., 2017; Dietrich et al., 2003; Galin et al., 2019; Heimsath et al., 2012; Jenness, 2004; R. Li, 2023; Liu et al., 2022; Lütjens et al., 2019; Montgomery, 2001; Pluymakers et al., 2017; Sofia et al., 2013; Sutton et al., 2022). Digital Terrain Models (DTMs) of the Earth surface are widely available and essential to test, quantify, and anticipate surface processes and properties, as well as their functional relationships. Common topographic metrics retrieved from DTMs are areal extent and slope angles (Blöthe et al., 2015; Burbank et al., 1996; Montgomery, 2001). These quantities are key parameters in engineering, economics, politics, material-, geo-, and bio-sciences to tackle challenges related to global and climatic changes (Church, 2010). However, those metrics have several (literal) shortcomings (Figure 1). In geomorphology, these shortcomings bias our view of Earth's topography as relatively flat (Willenbring et al., 2013).

To analyze 3D surfaces, their spatial data is remotely captured from one direction (Figure 1). The data is then projected onto 2D (x, y) grid cells. Each cell contains one value (z) representing the overall elevation of the area captured by the grid cell (Figure 1c). The slope is calculated by the difference in elevation (z) over the grid cell size (Berry, 2002). This approach has three main shortcomings.

First, capturing data in one orientation leads to inhomogeneous sampling with a lower data density on inclined surfaces to that view (Bernard et al., 2021). Vertical or overhanging slopes are not sampled at all. A consequence

Writing – original draft:
Anne Voigtländer
Writing – review & editing:
Aljoscha Rheinwalt, Stefanie Tofelde

of this is encountered in animations and topographic map services, where data or pixels on steep slopes seem stretched (Figure 1e). Second, the grid cell size L determines which slope angles can be resolved in a DTM (Smith et al., 2019). Third, projecting a 3D surface onto a 2D plane generates a geometric foreshortening (Figures 1a–1c). In DTMs, area is commonly calculated as the product of the number of cells times L (planform area hereafter). While horizontal landscapes are fully represented in the planform area, the surface area of inclined surfaces is shortened proportional to its slope (Figures 1b and 1d). We call this the projection error. In summary, steep surfaces are undersampled, less resolved and underrepresented in gridded DTMs (Figure 1d).

With an anticipated increase in sampling density leading to smaller DTM grid cells in the future (Sofia et al., 2013), topographic metrics are expected to improve as steeper slopes get resolved (Grieve et al., 2016; Larsen et al., 2014; Smith et al., 2019). The planform area remains widely unchanged. But the projection error, and thus the underrepresentation of steeper slopes and surface area, remains an unquantified and unresolved first-order error in DTM analysis at all resolutions (Figure 1).

The projection error, especially the underestimation of surface area, has been discussed in ecology, where processes and life happen on and along sloped surfaces (Dorner et al., 2002; Jenness, 2004). Observations of differences in surface length measures (Beasom et al., 1983; Hillier, 2007), surface area and volume estimates by slope (Berry, 2002; Doane et al., 2018; Dorner et al., 2002) have also been reported in geomorphology. Heuristic approaches to correct slope distributions (DiBiase et al., 2018) or surface area (Jenness, 2004) have been proposed. However, without analysis of the interrelation between surface area and slope distributions and quantification of the error, these approaches only had a marginal impact on DTM and pixel-based model analysis.

Here, we reason for and test an approach to correct for the projection error by applying it to synthetic landscapes with known slope distributions and surface areas. Although we focus on the projection error, we inevitably consider grid size effects, too. Applying the correction to real landscapes, we can compare topographic slope and area metrics to those derived by standard analysis. We analyze the corrected metrics in respect to the interpretation of Earth surface processes and landscape evolution.

2. Materials and Methods

2.1. Geometries of the Projection Error

The underrepresentation of inclined surfaces in planform view arises from the projection of remotely captured 3D data onto a 2D plane (Figures 1a–1c). Following trigonometry, the magnitude of this projection error is proportional to the cosine of the slope α[°](Figure 1d). The truncation of the surface area is by its inverse, 1/cos α.

2.1.1. Slope Calculation

Mathematically, the slope α is defined by

$$\alpha(x,y) = \tan^{-1}\left(\sqrt{\left(\frac{\partial z}{\partial x}\right)^2 + \left(\frac{\partial z}{\partial y}\right)^2}\right) \cdot 180°/\pi. \tag{1}$$

Different approaches to quantify dz/dx and dz/dy from gridded DTMs have been proposed (Horn, 1981; Travis, 1975; Zevenbergen & Thorne, 1987), and are widely implemented in GIS software (e.g., QGIS, ArcMap, SAGA) and topographic analysis packages (Grieve et al., 2016; Schwanghart & Scherler, 2014). Here, we use the four-neighbor method (Zevenbergen & Thorne, 1987) to calculate the slope for each grid cell, as it is closest to the analytical slope of functional landscapes (Smith et al., 2019).

2.1.2. Planform and Surface Area Calculations

The planform area of DTMs is the sum of all grid cells multiplied by their size L. The surface area is the area along the sloped surface, including changes in elevation z. For functional landscapes parameterized in (x, y), like synthetic ones, the analytical surface area, $A_{surface}$ can be derived by integrating $z(x, y)$ along x and y of each grid cell:

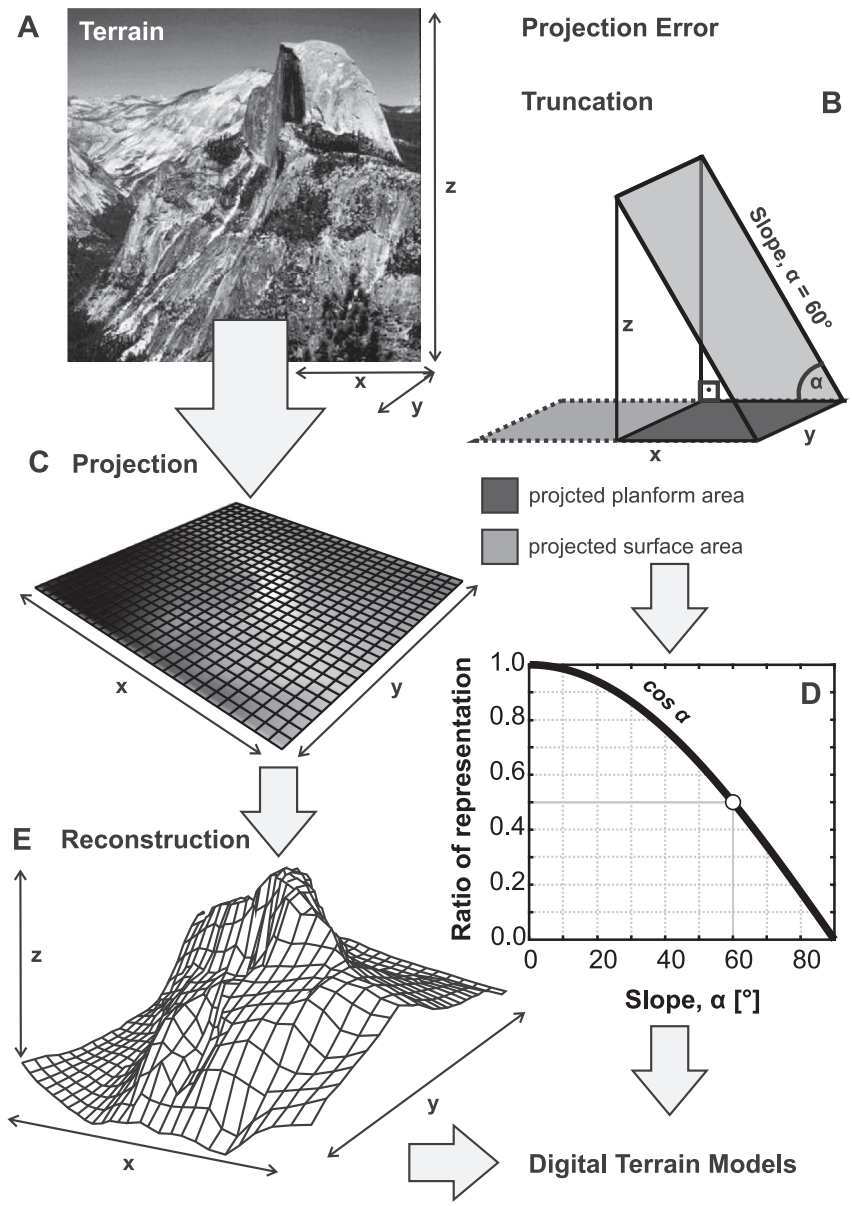

Figure 1. Projection error in Digital Terrain Models (DTMs). A Terrains are captured remotely from one orientation, and projected onto a planform surface, leading to a perspective foreshortening, and thus to a slope-dependent truncation, (b). (c) The projection represents the sloped surfaces only as a ratio, which is given by the cosine of the slope, (d). This leads to the projection error in surface area and slope distribution in DTMs. If reconstructed, the error shows as distortion of the grid cells, (e).

$$A_{surface} = \iint \left\| \frac{\partial \vec{r}}{\partial x} \times \frac{\partial \vec{r}}{\partial y} \right\| dx\, dy, \text{with } \vec{r} = (x, y, z(x,y)) \tag{2}$$

$$= \iint \left\| \left(1, 0, \frac{\partial z}{\partial x}\right) \times \left(0, 1, \frac{\partial z}{\partial y}\right) \right\| dx\, dy \tag{3}$$

$$= \iint \sqrt{1 + \left(\frac{\partial z}{\partial x}\right)^2 + \left(\frac{\partial z}{\partial y}\right)^2}\, dx\, dy \tag{4}$$

$$= \iint \frac{1}{\cos(\alpha(x,y))}\, dx\, dy. \tag{5}$$

If α is given (Equation 1), the surface area can easily be calculated following Equation 5. Otherwise, the surface area can be computed directly from the gradient along x and y following Equation 4.

Numerically integrating the surface area of natural landscapes with no functional form is computationally expensive. Approaches using discretized models, for example, Jenness, convert each grid cell into a Triangulated Irregular Network (TIN). By spanning eight triangles between the center point of a grid cell and its neighbors, the sum of all triangles' area overlapping the center cell serves as an approximation of its surface area (here called TINi).

Alternatively, we propose to use the mathematical formulation of surface area in terms of its slope α, referred to here as the COSi approach. This approach follows Equation 5, which can be approximated by 1/cos α, through which the area of each grid cell is weighted by its slope. We use the COSi corrected area to normalize the slope distribution. We call this approach hereafter "surface weighted." Slope distributions are usually normalized to the planform area, thus would be weighted by 1 (planform weighted). A similar approach to correct slope distributions, though by weighting the density kernel by 1/cos α, has been suggested by DiBiase et al. (2018).

2.2. Landscapes Put to Test

To test our COSi and the TINi approach to correct for the projection error in area and slope metrics, we generate synthetic landscapes (Hillier et al., 2015) for which surface area can be analytically calculated following Equation 5. To assess the effect of the projection error in natural landscapes, we pick two endmembers: the very steep area around Half Dome (HD) in Yosemite Valley and the gentle hills of the Gabilan Mesa (GM) area, both in California, USA. To test topographic metrics in relation to geomorphological processes, here the erosional response to uplift, we focus on catchments in the Mendocino Triple Junction (MTJ) area, California, USA.

We discretize both, synthetic and natural landscapes, at several resolutions and calculate the slope for each grid cell. We calculate TINi and COSi surface area and weigh the slope distributions accordingly. To compare the effect of the weighting, we display the slope distributions as probability density functions (PDFs). To quantify the deviation in area, we define the surface area ratio as surface area per planform area.

2.2.1. Synthetic Landscapes

We create two types of synthetic landscapes: Gaussian hills and CosSin landscapes based on superimposed sine and cosine functions. Each type is considered in a steep and a more gentle version, leading to four different synthetic landscapes in total. All of them cover a planform area of 1 km^2. The functional form of the Gaussian hill is given by

$$z(x,y) = \eta \cdot e^{-\frac{x^2+y^2}{2\sigma^2}} \tag{6}$$

with $\sigma^2 = 5 \cdot 10^4$ m^2, the origin being at the center of the tile and η being the height. We use this landscape with $\eta = 400$ m and $\eta = 200$ m. The functional form of the CosSin landscapes is given by

$$z(x,y) = \eta \cdot \cos\left(\frac{\pi x}{100}\right) \sin\left(\frac{\pi y}{100}\right) + \frac{\eta}{10} \cos\left(\frac{\pi x}{10}\right) \sin\left(\frac{\pi y}{10}\right) \tag{7}$$

with amplitudes η being either 50 m or 100 m. For the smaller wavelength part, the amplitude is scaled down by a factor of 10. For these synthetic landscapes we generate DTMs without noise and at an arbitrary resolution, by evaluating the functional form at each grid cell center.

2.2.2. Natural Landscapes

We generate bare-earth DTMs at different resolutions using airborne LiDAR scan point clouds. For the HD, GM, and MTJ area we retrieved ground-classified USGS 3DEP point clouds with average densities of 3.6 (HD), 4.5 (GM), and 1.4 (MTJ) ground points per m^2. From these point clouds, we derive DTMs with 1 m cell size using linear interpolation. For HD and GM we also derive DTMs with 5 and 30 m cell size. To discretize the MTJ area into individual catchments, we calculated river networks using the D8 algorithm (O'Callaghan & Mark, 1984) in

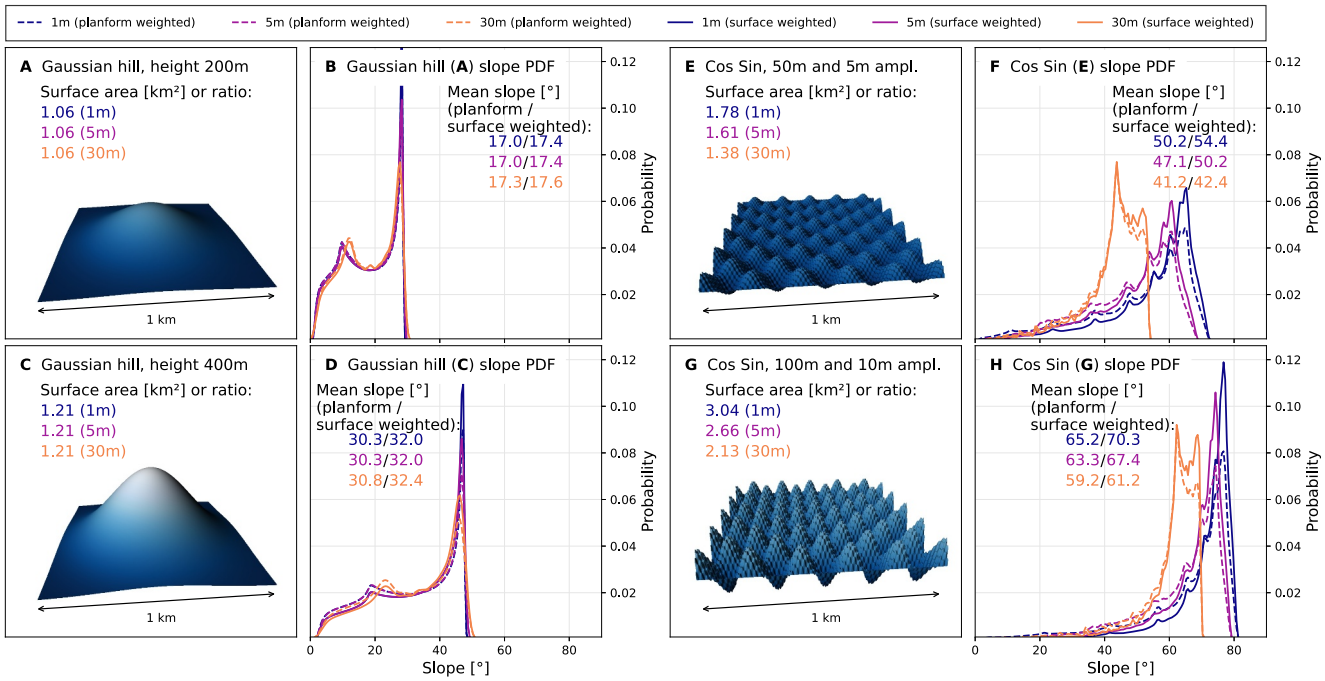

Figure 2. Synthetic landscapes, their true and COSi corrected surface area, or ratio to the planform area, and their slope PDFs at 1, 5, and 30 m resolution (colored, planform = dashed, surface weighted = solid lines). (a–d) display the topographic metrics of Gaussian hills, while (e and f) represent CosSin landscapes of two amplitudes each.

TopoToolbox (Schwanghart & Scherler, 2014) and extracted catchments upstream from river outlets close to the Pacific Ocean. The catchments largely overlap with those in Clubb et al. (2020), but extend further South.

3. Results

3.1. Synthetic Landscapes

For the synthetic landscapes, the surface area (km^2) or ratios are 1.06 for low and 1.21 for high amplitude Gaussian hills at all grid sizes. For the CosSin landscape, the ratios range from 1.38 to 1.78 for low amplitude and from 2.13 to 3.04 for high amplitude, depending on grid size (Figure 2). Both, COSi- and TINi-approaches, under- or overestimate the analytically derived surface area, but converge to the analytical solution with increasing grid resolution (Figures S1–S5 in Supporting Information S1). For the CosSin landscapes, the TINi-based approach seems to be closer to the analytical surface area than the COSi, as the large inter-grid cell variability balances itself out (Figure S3 in Supporting Information S1). However, due to the lower inter-grid cell variability, its relation to Equation 5, and the possibility to derive corrected slope distributions within the same correction, the COSi-approach is used herein.

We compare the surface weighted PDFs of the slope angles to the planform weighted PDFs to quantify the effect of the correction of the projection error. The PDFs of the Gaussian hills are bimodal, while the CosSin landscapes show rough and asymmetric, but more unimodal PDFs. Differences between planform and surface weighted slope PDFs increase the steeper and rougher the landscapes are (Figure 2). The mean slope increases from planform to surface weighted distributions at 1 m cell size by 0.4° in the gentle Gaussian hill, 1.7° in the steep Gaussian hill, and by 4.2° in the gentle CosSin and 5.1° in steep CosSin (Figures 2b, 2d, 2f, and 2h). Both slope distribution and surface area vary by resolution, with a general trend of steeper slopes and greater surface area at higher resolution (Figure 2), except for the surface area of the Gaussian hills (Figures 2a and 2c).

3.2. Natural Landscapes

We apply the COSi and surface weighting approach to two endmember topographies, the Half Dome (HD) and the Gabilan Mesa (GM, Figure 3). The surface area ratio of the steep HD ranges between 1.41 and 1.51 depending

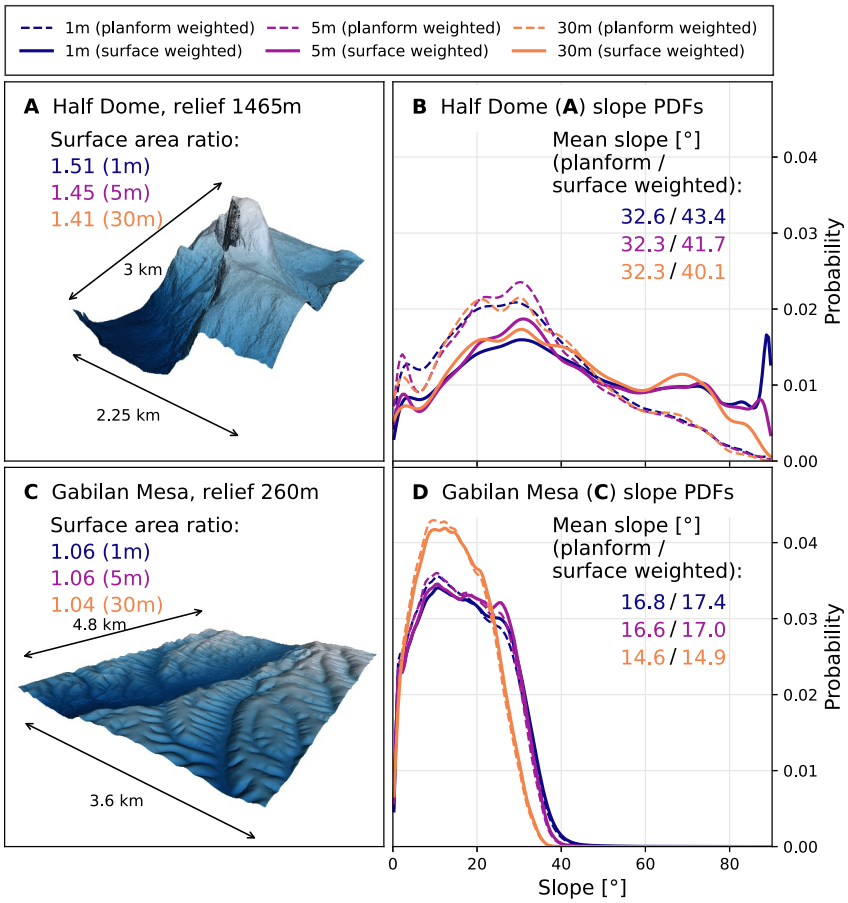

Figure 3. Surface area ratios and slope PDFs of Half Dome (a, b) and Gabilan Mesa (c, d) at 1, 5, and 30 m resolution (colored, planform = dashed, surface weighted = solid lines).

on the resolution, and translate to an areal difference of ~3 km^2 (Figure 3a). For the gentle GM, the surface area ratio is up to 1.06, which makes an areal difference of about 1 km^2 (Figure 3c). For HD, the surface weighted slope PDFs are multimodal and do not show a trend of decreasing density at increasing slope angle, as in the planform weighted PDFs, especially at higher resolutions (Figure 3b). The slope distributions of GM roughly follow unimodal distributions, which gets broader as resolution increases, and differ in the mean by 0.3–0.6° (Figure 3d).

3.3. DTMs and Earth Surface Processes

Topographic metrics are used as proxies for geomorphic processes in landscapes. Here we use the example of an erosional response to uplift. Uplift creates elevation, which increases slope angles and leads to higher erosion rates. It is assumed that erosion lowers the elevation difference and adjust the slope angles in the long-term to a mean of ~30° (Burbank et al., 1996; Montgomery, 2001). As such, the mean or median slope angle of a catchment can be seen as a proxy for uplift or erosion (Dietrich et al., 2003; Montgomery, 2001; Roering et al., 2001). We reassess the topographic metrics of catchments in the coastal mountain ranges off the Mendocino Triple Junction (MTJ) at 1 m grid size (Figure 4). The topographic metrics in this area have previously been interpreted to capture a northward migrating pulse of crustal thickening-related deformation causing uplift, and an equilibrating erosional response (Balco et al., 2013; Clubb et al., 2020; Merritts & Bull, 1989; Moon et al., 2018). Uplift rates increase in northward direction from 0.5 mm/yr (catchments 11–16) up to 4 mm/yr (catchments 30–36), before decreasing again to 3 mm/yr (catchments 42, 43) (Figure 4b). However, this spatial trend in uplift rates is not well matched by both the planform and surface weighted median slope of the catchments (Table S1 in Supporting Information S1, Figure 4d). We observe similar median slopes for catchments 8–38 of $\sim 30 - 34°$ despite the strong variation in uplift rates. But the region of highest uplift rates (catchments 27–39) corresponds with the highest values in the 90th percentiles of slope PDFs (Figures 4c and 4d) and in the surface area ratios (Figure 4b).

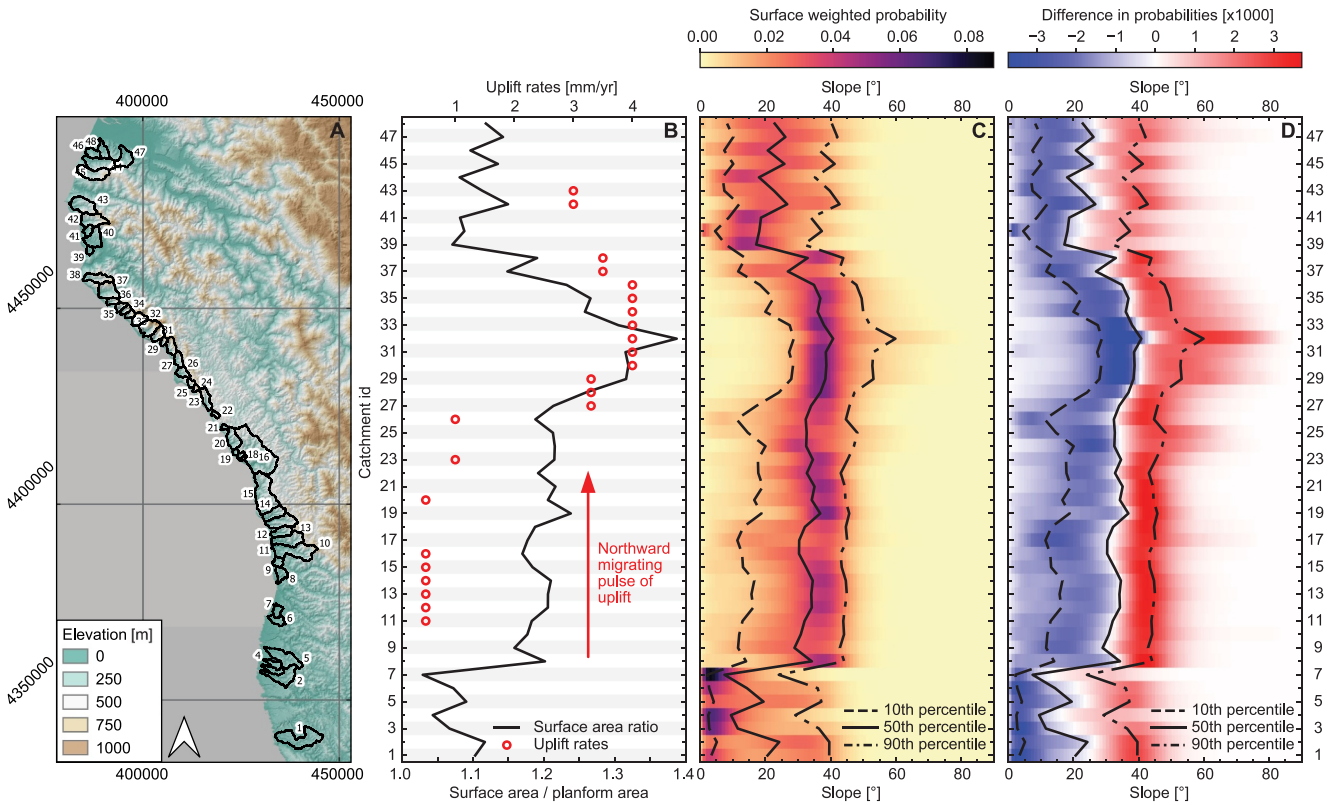

Figure 4. Topographic metrics of the Mendocino Triple Junction (MTJ) area and associated uplift. (a) Topographic map of the MTJ area, with catchment outlines. Catchments all drain to the Pacific and have planform areas of 1.50–71.08 km^2 (details in Supporting Information S1). (b) Surface area ratio for each catchment, and uplift rates, inferred from marine terraces (Merritts & Bull, 1989) and their numerical simulations (Clubb et al., 2020), where available. (c) Surface weighted slope PDFs displayed as heatplots for each of the 48 catchments, following a northward trend with increasing numbers. (d) Probability difference of planform minus surface-weighted PDFs, shown as bipolar heatplots for each catchment.

Southernmost catchments 1–8, as well as catchments 40–48 ahead of the main uplift pulse, show the opposite relation with the surface area ratios (Figure 4c). The zone of previous high, now lower uplift rates (catchments 8–26) still has surface area ratios of ∼1.2. These are higher than those (∼1.1) ahead of the highest uplift rates (catchments 39–48) and in the southernmost catchments (1–8). The greatest differences between the planform and surface weighted PDFs (Figure 4d), indicated by intense red color is found where the landscape is still responding to previous uplift pulse. In summary, using both the correction of the projection error and the surface area ratios (Figure 4c) we are able to clearly show the topographic response to the temporal and spatial variation of uplift and erosion.

4. Discussion

4.1. Earth's Surface Is Larger and Steeper Than Typically Thought

Gridded elevation models are still the primary way to characterize topography in Earth Sciences. While uncertainties related to grid resolution have been investigated (Grieve et al., 2016; Smith et al., 2019), the projection error remained largely unquantified. Our preferred COSi-correction inverts the foreshortening of the projection and represents all slopes equally in the distribution. Consequently, the mean or median shifts to higher slope angles. As corrections for the projections error are proportional to the slope, the effect on surface area and slope PDFs is strongest in rough and steep landscapes (Figures 2c–2h and 3a and 3b). For example, the mean slope increased in HD by ≥10° at 1 m grid spacing (Figure 3b). With technological advancements and processing abilities, steeper slopes can be resolved and the projection error will even get stronger (Figures 1d and 2e and 2g). However, even in gentle and smooth topography, the surface area is underestimated in both the synthetic 200 m Gaussian hill (Figure 2a) and GM (Figure 3c) by up to 6%.

While slope metrics generally increase with finer grid spacing or higher resolution (Larsen et al., 2014), our analysis shows this conclusion has four caveats. First, the degree to which the metrics shift depend on the difference in elevation relative to the grid resolution. For example, using the standard planform weighted approach, the mean slope of the gentle hills of GM shifts by 2.2° from 30 to 1 m cell size, while the steep terrain of HD changes only by 0.3° (Figures 3b and 3d). Similarly, in the CosSin landscape with smaller amplitudes (50 and 5 m) the mean slope increases by 9.0° from 30 to 1 m, compared to 6.0° in the steeper (100 and 10 m) case (Figures 2f and 2h). Higher grid resolution in gentle terrains resolves more small variations, while steeper inclines are still limited by the dependency on the grid resolution. This cutoff is, for example, in the steep CosSin landscape at ∼70° at 30 m, and at ∼80° at $1-5$ m grid size (Figure 2h). The stronger shift between 30 m and $1-5$ m resolution is that the 30 m is larger than our smaller wavelength of 20 m, and thus the slope fidelity zero (Grieve et al., 2016).

Second, if we account for the projection error in addition to the resolution, the trend of steepening at higher resolution saturates. For example, the surface area ratio of HD continuously increases with decreasing grid size from 1.41, to 1.45, to 1.51 (30, 5, 1 m), while for GM it remains at 1.06 at 5 and 1 m cell size (Figures 3a and 3c). The mean slope increases for both landscapes with higher grid resolution. The shift in HD from 30 to 1 m by 3.3° is much smaller than that by the correction of the projection error of 7.8° at 30 m, 9.4° at 5 m, and 10.8° at 1 m. However, for GM, the shift in the mean slope by resolution is 2.5°, while the surface weighting adds only 0.3°–0.6° (Figures 3b and 3d). This shows that landscapes may have a characteristic length scale (Grieve et al., 2016; Hillier et al., 2015).

Third, correcting for the projection error changes the shape of slope PDFs. Corrected PDFs from high resolution DTMs diverge more from a normal, symmetric, unimodal distribution than those extracted from coarse resolutions. Especially in steep terrain like the HD (Figure 3b), the corrected PDFs show multiple modes, skewness, and increased range.

Fourth, coarser resolution can lead to a decrease in the mean slope angle, as shown in the Gaussian hills (Figures 2b and 2d). The 200 m high Gaussian hill decreased in the mean by 0.3° from 1 to 30 m resolution, the 400 m hill by 0.5°, respectively. This is caused by discretization errors (Grieve et al., 2016). This caveat remains even if the truncation is reversed.

4.2. Effect on Distribution and Metrics

The comparison of the full slope distributions of the planform and surface weighted approaches, either in the PDFs (Figures 3b and 3d and 4a) or in the difference plots (Figure 4b), shows which slope angles are affected most. As many PDFs are neither unimodal nor normally distributed, the statistical prerequisites to calculate the mean slope are not fulfilled. For example, the Gaussian hills have a bimodal distribution, with maximum slopes of ∼30° or ∼50°, regardless of the weighting and resolution (Figures 2b and 2d). Even if the general distributions follow a more unimodal trend, as in the CosSin landscapes, they are not normal, but skewed (Figures 2f and 2h). We want emphasize that the apparent unimodal PDFs of uncorrected and coarser DTMs were used to establish the mean slope as a topographic indicator for slope stability and erosion (Burbank et al., 1996; Montgomery, 2001). The common usage of mean or median slope angles, even if corrected by surface weighting (DiBiase et al., 2018), might therefore be unfit to describe the distributions, and could further bias our interpretation of DTMs and related processes. Considering widths, shapes, percentiles, and modes of distributions (Figure 4), could offer improved insight into how landscapes evolve (Wolinsky & Pratson, 2005). For example, one could argue that the different modes in the slope distribution of the 1 m HD DTM indicate different process domains, for example, at $20-60°$ dominated by frictional hill slope processes, like debris flows and landslides; and >60° by bedrock processes, such as rock fall (Figures 3a and 3b).

4.3. Effect on the Interpretation of Earth Surface Processes

We are offering a shift in perspective that does not necessarily question existing interpretations of morphometric data. However, correcting the projection error allows for an estimation of the true surface area and leads to changes in slope distribution patterns. The underestimation of surface area by quantifying only the planform area is in the range of 20–30%, especially in steep terrains (Figure 3). In the MTJ area, the surface area ratio is ∼1.2 in the transition zone and ∼1.3 in the zone of highest uplift. In consequence, correcting the truncation also challenges how we imagine (e.g., flat (Willenbring et al., 2013)), conceptualize (e.g., threshold hillslopes (Montgomery, 2001)),

and interpret geomorphic metrics and surface processes (e.g., erosion rates, landslides (Bennett et al., 2016; Blöthe et al., 2015; Clubb et al., 2020; G. K. Li et al., 2022)).

In the MTJ, recognizing the spatial variability in uplift and accompanying geomorphic processes using the mean catchment slope is challenging due to similar values in the transition (catchments 9–26) and high uplift (catchments 27–39) zones. The mean slopes in these zones differ on average by 0.2° in the surface weighted and 0.04° in the planform weighted estimation (Table S1 in Supporting Information S1). Trying to interpret these metrics in terms of the dynamic equilibrium of uplift and erosion, as commonly done, renders a vague picture. However, using entire slope distributions and the new surface area ratio offers a more detailed picture. The northward migrating pulse of uplift increased elevation locally, hence created slopes and thus the potential for erosion. In response, slope distributions narrow and shift toward higher angles (catchments 27–39, Figure 4c). Once the uplift rate ceased, erosional and depositional processes set in and impact the topographic metrics. Slope distribution broaden and expand toward gentler slopes (catchments 9–27). In the long-term, erosion dominates and shifts the slope distributions to low angles (catchments 1–8). Catchments 40–47 ahead of highest uplift rates are characterized by overall low slopes (Figure 4c). In our analysis, the topographic expression of the erosional response to uplift is best detected by the surface area ratio (Figure 4b). To interpret the processes, the changes in the width range, modality, and the high percentile of the slope distribution provide further parameters. Utilizing the corrected topographic metrics allows addressing relations like distribution of dominant gravitational processes by slopes, or potentials for erosion based on surface area. Exploring these relationships allows deriving and testing physics based erosion and transport laws.

5. Conclusion

Introducing the surface area ratio enables determining the effectiveness of Earth surface processes, by increasing or decreasing the differential between the planform and the surface area, like in our example of an erosional response to uplift in the MTJ area (Figure 4c). Earth surface processes, that involve transport and volume along the surfaces, if not referenced in time, the ratio between the planform and surface area can provide a spatial reference and could be explored further. The surface weighting approach enables a more correct representation of 3D surfaces in models and data, from which topographic gradients, like slope angles, length and area can be retrieved. These metrics can then feed into calculating, for example, potential kinetic energy, mass, transport distance and rates, and frictional loss. All of these provide the base for a mechanistic and physically sound interpretation of topography as a proxy for surface processes. Especially in non-local transport processes, like groundwater flow or diffusion, the travel distance depends on the true slope length (Perreault et al., 2017; Roth et al., 2020; Voller et al., 2012), and to estimate erosion rates (Wang & Willett, 2021) or volumes (Doane et al., 2018), the true surface area is needed. Reverting the truncation might require revisiting some established concepts and correlations, such as landscape roughness and age (LaHusen et al., 2016; Montgomery, 2001), threshold hill slopes, and excess topography (Blöthe et al., 2015; Burbank et al., 1996; Dietrich et al., 2003; Egholm et al., 2009; G. K. Li et al., 2022). However, as the physical interpretation of the surface processes, relies on the relative motion of a mass to a surface, for example, surface runoff, gravitational mass movements; some related processes, such as precipitation, incident cosmic or solar rays, which are commonly assumed orthogonal to the planform (Balco et al., 2013; Moon et al., 2018; Riebe et al., 2015), might not be affected by the projection error.

The topography of the Earth does not conform to a simple mathematical shape—so there is an error in trying to squeeze it into regular geometries. Given that DTMs are what we have, and as shown here, a simple method to account for and mitigate the projection error can still provide relevant answers to surface area and slope-related processes at any scale.

Data Availability Statement

We tried to use data sources that are widely accessible by the community through open access data servers, like OpenTopography, and USGS, as well as published data sets for example, (Clubb et al., 2020). To ease the application of the suggested approaches to correct for the projection error in your data, all scrips can be found here: (https://github.com/UP-RS-ESP/dtm-surface-area-and-slope). Supporting Information S1 contains additional Figures S1–S6 in Supporting Information S1 comparing the COSi and TINi approach, Figures S7–S54 in

Supporting Information S1 detail the slope maps and PDFs of all catchments of Figure 4, further summarized in Table S1 in Supporting Information S1.

Acknowledgments
This paper highly benefited from discussions with B. Brokhagen, J.M. Turowski, T. Smith, N. Hovius, F. Clubb, and E. Orr. We thank the reviewers S. Mudd and J.K. Hillier for their constructive comments. Open Access funding enabled and organized by Projekt DEAL.

References

Balco, G., Finnegan, N., Gendaszek, A., Stone, J. O., & Thompson, A. (2013). Erosional response to northward-propagating crustal thickening in the coastal ranges of the U.S. Pacific Northwest. *American Journal of Science*, *313*(8), 790–806. https://doi.org/10.2475/11.2013.01

Beasom, S. L., Wiggers, E. P., & Giardino, J. R. (1983). A technique for assessing land surface ruggedness. *Journal of Wildlife Management*, *47*(4), 1163. https://doi.org/10.2307/3808184

Bennett, G. L., Miller, S. R., Roering, J. J., & Schmidt, D. A. (2016). Landslides, threshold slopes, and the survival of relict terrain in the wake of the Mendocino Triple Junction. *Geology*, *44*(5), 363–366. https://doi.org/10.1130/G37530.1

Bernard, T. G., Lague, D., & Steer, P. (2021). Beyond 2d landslide inventories and their rollover: Synoptic 3d inventories and volume from repeat lidar data. *Earth Surface Dynamics*, *9*(4), 1013–1044. https://doi.org/10.5194/esurf-9-1013-2021

Berry, J. K. (2002). Beyond mapping: Use surface area for realistic calculations. *GeoWorld*, *15*(9), 22–23.

Blöthe, J. H., Korup, O., & Schwanghart, W. (2015). Large landslides lie low: Excess topography in the Himalaya-Karakoram ranges. *Geology*, *43*(6), 523–526. https://doi.org/10.1130/G36527.1

Brodsky, E. E., Kirkpatrick, J. D., & Candela, T. (2016). Constraints from fault roughness on the scale-dependent strength of rocks. *Geology*, *44*(1), 19–22. https://doi.org/10.1130/G37206.1

Burbank, D., Leland, J., Fielding, E., Anderson, R. S., Brozovic, N., Reid, M. R., & Duncan, C. (1996). Bedrock incision, rock uplift and threshold hillslopes in the northwestern Himalayas. *Nature*, *379*(6565), 505–510. https://doi.org/10.1038/379505a0

Church, M. (2010). The trajectory of geomorphology. *Progress in Physical Geography*, *34*(3), 265–286. https://doi.org/10.1177/0309133310363992

Clubb, F. J., Mudd, S. M., Hurst, M. D., & Grieve, S. W. (2020). Differences in channel and hillslope geometry record a migrating uplift wave at the Mendocino triple junction, California, USA. *Geology*, *48*(2), 184–188. https://doi.org/10.1130/G46939.1

DiBiase, R. A., Lamb, M. P., Ganti, V., & Booth, A. M. (2017). Slope, grain size, and roughness controls on dry sediment transport and storage on steep hillslopes. *Journal of Geophysical Research: Earth Surface*, *122*(4), 941–960. https://doi.org/10.1002/2016JF003970

DiBiase, R. A., Rossi, M. W., & Neely, A. B. (2018). Fracture density and grain size controls on the relief structure of bedrock landscapes. *Geology*, *46*(5), 399–402. https://doi.org/10.1130/G40006.1

Dietrich, W. E., Bellugi, D. G., Sklar, L. S., Stock, J. D., Heimsath, A. M., & Roering, J. J. (2003). Geomorphic transport laws for predicting landscape form and dynamics. *Geophysical Monograph Series*, *135*, 103–132. https://doi.org/10.1029/135GM09

Doane, T. H., Furbish, D. J., Roering, J. J., Schumer, R., & Morgan, D. J. (2018). Nonlocal sediment transport on steep lateral Moraines, Eastern Sierra Nevada, California, USA. *Journal of Geophysical Research: Earth Surface*, *123*(1), 187–208. https://doi.org/10.1002/2017JF004325

Dorner, B., Lertzman, K., & Fall, J. (2002). Landscape pattern in topographically complex landscapes: Issues and techniques for analysis. *Landscape Ecology*, *17*(8), 729–743. https://doi.org/10.1023/A:1022944019665

Egholm, D. L., Nielsen, S. B., Pedersen, V. K., & Lesemann, J. (2009). Glacial effects limiting mountain height. *Nature*, *460*, 884–887. https://doi.org/10.1038/nature08263

Galin, E., Guérin, E., Peytavie, A., Cordonnier, G., Cani, M.-P., Benes, B., & Gain, J. (2019). A review of digital terrain modeling. *Computer Graphics Forum*, *38*(2), 553–577. https://doi.org/10.1111/cgf.13657

Grieve, S. W. D., Mudd, S. M., Milodowski, D. T., Clubb, F. J., & Furbish, D. J. (2016). How does grid-resolution modulate the topographic expression of geomorphic processes? *Earth Surface Dynamics*, *4*(3), 627–653. https://doi.org/10.5194/esurf-4-627-2016

Heimsath, A. M., DiBiase, R. A., & Whipple, K. X. (2012). Soil production limits and the transition to bedrock-dominated landscapes. *Nature Geoscience*, *5*(3), 210–214. https://doi.org/10.1038/ngeo1380

Hillier, J. K. (2007). Pacific seamount volcanism in space and time. *Geophysical Journal International*, *168*(2), 877–889. https://doi.org/10.1111/j.1365-246X.2006.03250.x

Hillier, J. K., Sofia, G., & Conway, S. J. (2015). Perspective—Synthetic DEMs: A vital underpinning for the quantitative future of landform analysis? *Earth Surface Dynamics*, *3*(4), 587–598. https://doi.org/10.5194/esurf-3-587-2015

Horn, B. K. (1981). Hill shading and the reflectance map. *Proceedings of the IEEE*, *69*(1), 14–47. https://doi.org/10.1109/proc.1981.11918

Jenness, J. S. (2004). Calculating landscape surface area from digital elevation models. *Wildlife Society Bulletin*, *32*(3), 829–839. https://doi.org/10.2193/0091-7648(2004)032[0829:clsafd]2.0.co;2

LaHusen, S. R., Duvall, A. R., Booth, A. M., & Montgomery, D. R. (2016). Surface roughness dating of long-runout landslides near Oso, Washington (USA), reveals persistent postglacial hillslope instability. *Geology*, *44*(2), 111–114. https://doi.org/10.1130/G37267.1

Larsen, I. J., Montgomery, D. R., & Greenberg, H. M. (2014). The contribution of mountains to global denudation. *Geology*, *42*(6), 527–530. https://doi.org/10.1130/G35136.1

Li, G. K., Moon, S., & Higa, J. T. (2022). Residence time of over-steepened rock masses in an active mountain range. *Geophysical Research Letters*, *49*(7), 1–10. https://doi.org/10.1029/2021gl097319

Li, R. (2023). Real-world large-scale terrain model reconstruction and real-time rendering. In *Proceedings of the 28th International ACM Conference on 3D Web Technology*. Association for Computing Machinery. https://doi.org/10.1145/3611314.3615901

Liu, S., Kuhn, C., Amatulli, G., Aho, K., Butman, D. E., Allen, G. H., et al. (2022). The importance of hydrology in routing terrestrial carbon to the atmosphere via global streams and rivers. *Proceedings of the National Academy of Sciences of the United States of America*, *119*(11), 1–9. https://doi.org/10.1073/pnas.2106322119

Lütjens, M., Kersten, T. P., Dorschel, B., & Tschirschwitz, F. (2019). Virtual reality in cartography: Immersive 3d visualization of the Arctic Clyde Inlet (Canada) using digital elevation models and bathymetric data. *Multimodal Technologies and Interaction*, *3*(1), 9. https://doi.org/10.3390/mti3010009

Merritts, D., & Bull, W. B. (1989). Interpreting Quaternary uplift rates at the Mendocino triple junction, northern California, from uplifted marine terraces. *Geology*, *17*(11), 1020–1024. https://doi.org/10.1130/0091-7613(1989)017⟨1020:IQURAT⟩2.3.CO;2

Montgomery, D. R. (2001). Slope distributions, threshold hillslopes, and steady-state topography. *American Journal of Science*, *301*(4–5), 432–454. https://doi.org/10.2475/ajs.301.4-5.432

Moon, S., Merritts, D. J., Snyder, N. P., Bierman, P., Sanquini, A., Fosdick, J. C., & Hilley, G. E. (2018). Erosion of coastal drainages in the Mendocino Triple Junction region (MTJ), northern California. *Earth and Planetary Science Letters*, *502*, 156–165. https://doi.org/10.1016/j.epsl.2018.09.006

O'Callaghan, J. F., & Mark, D. M. (1984). The extraction of drainage networks from digital elevation data. *Computer Vision, Graphics, and Image Processing*, *28*(3), 323–344. https://doi.org/10.1016/s0734-189x(84)80011-0

Perreault, L. M., Yager, E. M., & Aalto, R. (2017). Effects of gradient, distance, curvature and aspect on steep burned and unburned hillslope soil erosion and deposition. *Earth Surface Processes and Landforms*, *42*(7), 1033–1048. https://doi.org/10.1002/esp.4067

Pluymakers, A., Kobchenko, M., & Renard, F. (2017). How microfracture roughness can be used to distinguish between exhumed cracks and in-situ flow paths in shales. *Journal of Structural Geology*, *94*, 87–97. https://doi.org/10.1016/j.jsg.2016.11.005

Riebe, C. S., Sklar, L. S., Lukens, C. E., & Shuster, D. L. (2015). Climate and topography control the size and flux of sediment produced on steep mountain slopes. *Proceedings of the National Academy of Sciences of the United States of America*, *112*(51), 15574–15579. https://doi.org/10.1073/pnas.1503567112

Roering, J. J., Kirchner, J. W., & Dietrich, W. E. (2001). Hillslope evolution by nonlinear, slope-dependent transport: Steady state morphology and equilibrium adjustment timescales. *Journal of Geophysical Research*, *106*(B8), 16499–16513. https://doi.org/10.1029/2001jb000323

Roth, D. L., Doane, T. H., Roering, J. J., Furbish, D. J., & Zettler-Mann, A. (2020). Particle motion on burned and vegetated hillslopes. *Proceedings of the National Academy of Sciences of the United States of America*, *117*(41), 25335–25343. https://doi.org/10.1073/pnas.1922495117

Schwanghart, W., & Scherler, D. (2014). Short communication: TopoToolbox 2—MATLAB-based software for topographic analysis and modeling in Earth surface sciences. *Earth Surface Dynamics*, *2*(1), 1–7. https://doi.org/10.5194/esurf-2-1-2014

Smith, T., Rheinwalt, A., & Bookhagen, B. (2019). Determining the optimal grid resolution for topographic analysis on an airborne lidar dataset. *Earth Surface Dynamics*, *7*(2), 475–489. https://doi.org/10.5194/esurf-7-475-2019

Sofia, G., Pirotti, F., & Tarolli, P. (2013). Variations in multiscale curvature distribution and signatures of lidar DTM errors. *Earth Surface Processes and Landforms*, *38*(10), 1116–1134. https://doi.org/10.1002/esp.3363

Sutton, S. S., Chojnacki, M., McEwen, A. S., Kirk, R. L., Dundas, C. M., Schaefer, E. I., et al. (2022). Revealing active mars with hirise digital terrain models. *Remote Sensing*, *14*(10), 2403. https://doi.org/10.3390/rs14102403

Travis, M. R. (1975). In *Viewit: Computation of seen areas, slope, and aspect for land-use planning* (Vol. 11). Department of Agriculture, Forest Service, Pacific Southwest Forest and Range Experiment Station.

Voller, V. R., Ganti, V., Paola, C., & Foufoula-Georgiou, E. (2012). Does the flow of information in a landscape have direction? *Geophysical Research Letters*, *39*(1), 1–5. https://doi.org/10.1029/2011GL050265

Wang, Y., & Willett, S. (2021). Escarpment retreat rates derived from detrital cosmogenic nuclide concentrations. *Earth Surface Dynamics Discussions*, 1–38. https://doi.org/10.5194/esurf-2021-27

Willenbring, J. K., Codilean, A. T., & McElroy, B. (2013). Earth is (mostly) flat: Apportionment of the flux of continental sediment over millennial time scales. *Geology*, *41*(3), 343–346. https://doi.org/10.1130/G33918.1

Wolinsky, M. A., & Pratson, L. F. (2005). Constraints on landscape evolution from slope histograms. *Geology*, *33*(6), 477–480. https://doi.org/10.1130/G21296.1

Zevenbergen, L. W., & Thorne, C. R. (1987). Quantitative analysis of land surface topography. *Earth Surface Processes and Landforms*, *12*(1), 47–56. https://doi.org/10.1002/esp.3290120107